



# Synthesis and performance of ceria-zirconia supported Ni-Mo nanoparticles for partial oxidation of isooctane

Qusay Bkour<sup>a</sup>, Kai Zhao<sup>a</sup>, Louis Scudiero<sup>b</sup>, Da Jung Han<sup>c</sup>, Chang Won Yoon<sup>c</sup>, Oscar G. Marin-Flores<sup>d</sup>, M. Grant Norton<sup>d,\*</sup>, Su Ha<sup>a,\*</sup>

<sup>a</sup> Voiland School of Chemical Engineering and Bioengineering, Washington State University, Pullman, WA, 99164, USA

<sup>b</sup> Chemistry Department and Materials Science and Engineering Program, Washington State University, Pullman, WA, 99164, USA

<sup>c</sup> Fuel Cell Research Center, Korea Institute of Science and Technology, Seoul, 02792, Republic of Korea

<sup>d</sup> School of Mechanical and Materials Engineering, Washington State University, Pullman, WA, 99164, USA

## ARTICLE INFO

### Article history:

Received 20 February 2017

Received in revised form 9 April 2017

Accepted 20 April 2017

Available online 23 April 2017

### Keywords:

Ni-Mo nanoparticles

Partial oxidation

Isooctane

Micro-reforming layer

SOFC

## ABSTRACT

Catalyst deactivation due to sintering and carbon deposition is one of the main issues associated with electrocatalysis and catalytic hydrocarbon reforming over supported Ni catalysts. We report a Ni-Mo bimetallic catalyst supported on ceria-zirconia (CZ) prepared using co-impregnation as an efficient catalyst for partial oxidation of isooctane at high space velocities. It is also used as a catalytic micro-reforming layer on a conventional Ni/YSZ-based solid oxide fuel cell (SOFC) to form a bi-layer anode. The catalysts were characterized using a number of analytical techniques and catalyst performance for partial oxidation of isooctane was investigated at 750 °C; atmospheric pressure; air and fuel flow rates of 100 sccm and 3 ml/h, respectively; and O<sub>2</sub>/C ratio of 0.4. The addition of Mo increases the catalytic activity in terms of isooctane conversion and syngas yields. Most significantly, the presence of Mo enhances the long-term stability of the Ni-based catalyst. Molybdenum strengthens the interaction between Ni and the support and improves the overall metal dispersion. We have further demonstrated that the carbon tolerance of Ni can be significantly improved by Mo addition. When applied it as a reforming layer in a SOFC running on isooctane, the cell showed a very slow degradation rate of 4.8 mV h<sup>-1</sup> during 12 h of operation at 750 °C. The excellent catalytic activity and stability suggest that Ni-Mo/CZ is an excellent material for a bi-layer anode of SOFC with superior coke tolerance.

© 2017 Elsevier B.V. All rights reserved.

## 1. Introduction

Every day millions of gallons of oil are consumed for transportation purposes alone [1]. International concerns over the environmental effects of CO<sub>2</sub> emissions from the combustion of fossil fuels recently culminated in the signing of the Paris Agreement by 195 countries with the goal of limiting the effect of global warming to less than 2 °C compared to pre-industrial levels [2]. To meet this goal, more efficient and sustainable approaches are needed. Hydrogen fuel cells are often cited as a solution since they can directly convert the chemical energy of hydrogen into electrical energy with a high efficiency [3]. However, several problems limit the effectiveness of conventional fuel cells. Among them are logistical problems associated with the lack of a hydrogen infrastructure as well as high costs associated with hydrogen distribution

and storage [4]. One solution to these problems is to use logistic liquid fuels (e.g., gasoline, diesel, biodiesel, and kerosene-based jet fuels) as a hydrogen storage medium. These fuels can be easily transported and stored using existing infrastructures and reformed *in-situ* into H<sub>2</sub> to power a fuel cell when the electrical energy is needed. Current methods for fuel reforming involve external fuel processors, which increase the device footprint and add complexity to the overall fuel cell system [5]. Unlike these external fuel processor-based fuel cell systems, internal reforming SOFCs can be operated by directly feeding the liquid fuel to the anode without externally reforming the fuel into syngas. Thus, so called “internal reforming SOFCs” can convert chemical energy into electrical energy with high overall fuel efficiency [6], while providing both space and weight benefits because of the smaller footprint and simpler design [7].

In order to realize liquid fuel internal reforming SOFC technology the anode material and design must efficiently reform the liquid fuel into syngas followed by electrochemical oxidation while preventing coke formation. To meet these requirements one can

\* Corresponding authors.

E-mail addresses: [mg.norton@wsu.edu](mailto:mg.norton@wsu.edu) (M.G. Norton), [suha@wsu.edu](mailto:suha@wsu.edu) (S. Ha).

introduce a catalytic micro-reforming layer over the conventional Ni/YSZ-based cermet anode. Zhan et al. [4] used a Ru-CeO<sub>2</sub> catalyst layer and found that the cell was much more stable than without the catalyst layer. Any realistic alternative energy solution must be cost effective. Thus, noble metal-based anode materials needs to be avoided. Nickel (Ni)-based anodes have good catalytic activity and stability for reforming low molecular weight hydrocarbons, but tend to suffer from coke formation and sintering with higher molecular weight fuels – both of which are detrimental to the long-term stability of the fuel cells [8,9]. Modifying the catalyst support and introducing additives can improve the activity and stability of Ni catalysts. The interaction between the active metal and the support affects the catalyst performance by changing the properties of the active phase such as its reducibility and dispersion [10].

Metal oxides with enhanced oxygen storage capacity (OSC) and oxygen vacancies were utilized to facilitate the removal of carbon deposits and enhance Ni metal dispersion [11]. Among them, catalytic materials based on pure and metal-doped ceria-zirconia (CZ) solid solutions have been widely investigated for enhancing both activity and stability of methane reforming [12–14]. The ability of CZ to switch between two oxidation states (3+ and 4+) and the large concentration of vacancies in the solid solution lead to both a high OSC and a high redox activity, which enables a high tolerance toward coking [15–17]. Shan et al. [18] studied the partial oxidation of methane over a Ni/CZ catalyst and demonstrated good activity and coking resistance over 20 h of operation. Astrid et al. [15] found that the formation of filamentous carbon was strongly reduced after using Ni/CZ for methane dry reforming. Claudia et al. [19] found that Mo species increased the coking resistance of Ni-Mo/Al<sub>2</sub>O<sub>3</sub> catalysts. Our group recently showed that SiO<sub>2</sub>-supported MoO<sub>2</sub> nanoparticle catalysts had good stability for the partial oxidation of *n*-dodecane for 24 h of operation without any sign of deactivation [20]. Shah et al. also reported the good activity and stability of Ni-Mo alloy supported on Mo<sub>2</sub>C for partial oxidation of methyl oleate (a surrogate biodiesel) [21].

The objective of this present research is to develop a SOFC capable of reforming liquid fuel (specifically isooctane) using active, coking-tolerant, and stable Ni-based bimetallic nanoparticles with Mo promoter as an internal reforming layer at high fuel and air flow rates. The Ni-Mo/CZ internal reforming layer was synthesized by wet co-impregnation and applied over a conventional Ni-YSZ-based SOFC electrode to form a bi-layer anode. The effect of zirconia in the ceria matrix as well as the effect of Ni-Mo bimetallic formulation on the catalytic performance for partial oxidation of isooctane was emphasized. This work elucidates the nature of Mo promotion, the nature of the metal-support interaction, and how this interaction changes the activity and stability of the catalyst.

## 2. Experimental

### 2.1. Catalyst synthesis and single cell fabrication

Commercial ceria-zirconia (Ce<sub>0.75</sub>Zr<sub>0.25</sub>O<sub>2</sub> (CZ), Aldrich) was used to prepare Ni-Mo/CZ by wet co-impregnation, in which the Ni content was kept at 11 wt.% and the Mo content was varied between 0 and 3 wt.%. An aqueous solution of (Ni (NO<sub>3</sub>)<sub>2</sub>·6H<sub>2</sub>O, Alfa Aesar) and ((NH<sub>4</sub>)<sub>6</sub>Mo<sub>7</sub>O<sub>24</sub>·4H<sub>2</sub>O, Alfa Aesar) was mixed with the CZ support and stirred at 70 °C until it forms a viscous mixture. The samples were then dried overnight at 100 °C, calcined at 500 °C for 4 h and then reduced at 750 °C for 1.5 h in a flowing 50% H<sub>2</sub>/He mixture. The resulting materials are referred to as Ni-Mo (X%)/CZ (where X is the Mo metal wt.%). Commercial ceria oxide (99.5%, Alfa Aesar) was compared with CZ.

SOFC single cells with a configuration of Ni-YSZ anode/YSZ/Ce<sub>0.8</sub>Sm<sub>0.2</sub>O<sub>1.9</sub> bi-layer

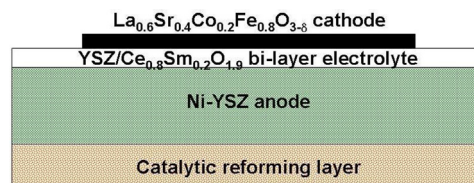


Fig. 1. Schematic diagram of the single Ni/YSZ-based anode supported cell with catalytic reforming layer.

electrolyte/La<sub>0.6</sub>Sr<sub>0.4</sub>Co<sub>0.2</sub>Fe<sub>0.8</sub>O<sub>3-δ</sub> cathode were fabricated by dry pressing and spin coating. The NiO-YSZ powder was ball milled with 15 wt.% corn starch (Sigma Aldrich), pressed into 15 mm diameter pellets at 60 MPa, and calcined at 1000 °C for 3 h. The YSZ/Ce<sub>0.8</sub>Sm<sub>0.2</sub>O<sub>1.9</sub> bi-layer electrolyte was deposited by slurry spin coating as follows. 17 wt.% YSZ powder (Inframat Advanced Materials) was mixed with 24.9 wt.% B73210 organic binder (Ferro Electronics), 33.2 wt.% terpineol (Sigma Aldrich) and 24.9 wt.% ethanol (Decon Laboratories) forming a slurry. The YSZ slurry was spin coated onto the NiO-YSZ substrates at 3000 rpm for 40 s (KW-4A, MicroNano Tools). This process was repeated twice to form a layer with the desired thickness. The Ce<sub>0.8</sub>Sm<sub>0.2</sub>O<sub>1.9</sub> layer was deposited on the surface of YSZ layer in the same way. Then the NiO-YSZ substrate with the YSZ/Ce<sub>0.8</sub>Sm<sub>0.2</sub>O<sub>1.9</sub> bi-layer electrolyte was co-sintered at 1400 °C for 4 h in air. The detailed fabrication process has been reported elsewhere [22]. The La<sub>0.6</sub>Sr<sub>0.4</sub>Co<sub>0.2</sub>Fe<sub>0.8</sub>O<sub>3-δ</sub> cathode layer was fabricated on the Ce<sub>0.8</sub>Sm<sub>0.2</sub>O<sub>1.9</sub> electrolyte layer by a similar spin-coating process. 14.1 wt.% La<sub>0.6</sub>Sr<sub>0.4</sub>Co<sub>0.2</sub>Fe<sub>0.8</sub>O<sub>3-δ</sub> powder (Fuel Cell Materials) was mixed with 0.8 wt.% ethyl cellulose (Sigma Aldrich) and 85.1 wt.% ethanol to make the cathode slurry. The slurry was spin-coated onto the Ce<sub>0.8</sub>Sm<sub>0.2</sub>O<sub>1.9</sub> electrolyte at 3000 rpm for 40 s and sintered at 1000 °C for 2 h in air.

The Ni-Mo/CZ catalyst was applied onto the porous YSZ substrate (thickness: ~0.5 mm) as an internal reforming layer for the single cell running on isooctane as follows. 25 wt.% corn starch pore former was ball milled with 75 wt.% YSZ powder. The mixture was compressed into 15 mm diameter pellets at 60 MPa. The green pellets were sintered at 1400 °C for 2 h to obtain the porous YSZ substrates. To coat the Ni-Mo/CZ catalyst onto the YSZ substrate, 10 wt.% Ni-Mo/CZ catalyst was mixed with 5 wt.% ethyl cellulose and 85 wt.% terpineol to make a slurry. The slurry was painted on both sides of the YSZ substrate for the catalytic reforming layer of the single cell to produce the configuration shown in Fig. 1.

### 2.2. Catalyst characterization

The surface area of the prepared samples was measured by N<sub>2</sub> adsorption using the single point BET method with a Chemisorb 2720 equipped with a thermal conductivity detector (TCD). The system was purged and calibrated before every analysis. All samples were degassed at 250 °C for 1 h before recording a measurement. The crystalline phases of the catalytic materials were determined by X-ray diffraction (XRD) using a Rigaku (Miniflex 600) with Cu Kα radiation operated at 40 kV, 15 mA in steps of 0.01° with a scanning rate at 1 °C/min from 20° to 60°. Jade software was used for peak identification. The reducibility of the samples was measured by temperature-programmed reduction (TPR): 100 mg of sample was placed in a U-shaped quartz tube and pretreated with flowing He at rate of 50 ml/min. Following the pretreatment, 10% H<sub>2</sub>/He was introduced at the same flow rate in the temperature range 25–900 °C with heating rate of 10 °C/min. Transmission electron microscopy (TEM) was used to investigate the morphologies of the catalytic materials using a FEI Technai G2 20 Twin at 200 kV. The morphology of the materials was characterized by high-resolution

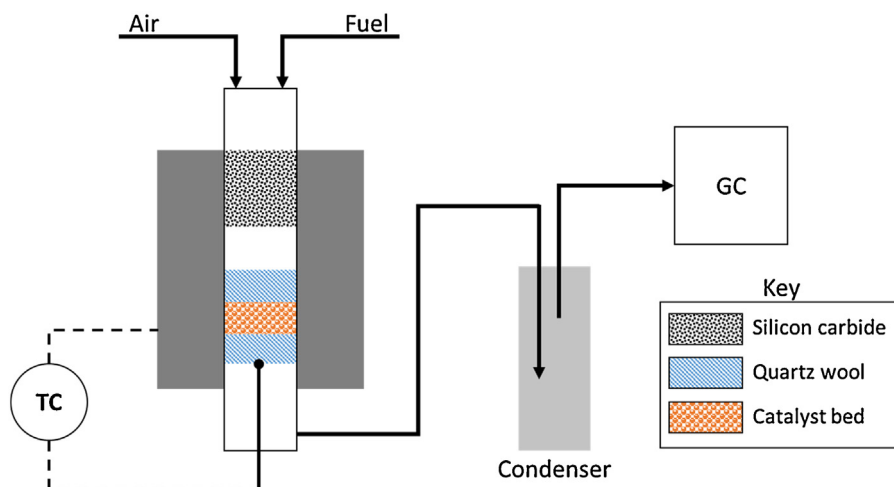


Fig. 2. Schematic diagram for partial oxidation experimental setup.

transmission electron microscopy (HRTEM, FEI Tecnai F20) and high-angle annular dark field (HAADF) microscopy (Talos F200X), coupled with scanning transmission electron microscopy (STEM) and energy dispersive spectroscopy (EDS) for elemental mapping at 200 kV. The samples for STEM were prepared by dispersing them in ethanol and drop casting these materials on carbon film 200 mesh copper grid (CF200-Cu, Electron Microscopy Sciences).

Oxygen storage capacity (OSC) was measured by placing 50 mg of catalyst in a quartz tube. The sample was preheated at 750 °C for 30 min under flowing He. Pulses of H<sub>2</sub> were injected every 5 s at 750 °C up to 30 pulses. The consumption of H<sub>2</sub> was analyzed using a 5975C Agilent Technologies mass spectrometer with triple-axis detector. The amount of O<sub>2</sub> per mass of catalyst is calculated according to the consumption of the H<sub>2</sub> pulses, and the first pulse represents the OSC value. The summation of OSC of the catalysts of the first 10 pulses is the cumulative oxygen storage capacity (COSC) that represents the total amount of O<sub>2</sub> available in the oxide support.

The metal dispersion was measured using CO pulse chemisorption, in which the sample was flushed with 50 ml/min Ar for 30 min at room temperature and the flow was switched to 50% H<sub>2</sub>/Ar at a rate of 50 ml/min for 30 min after increasing the temperature to 300 °C to remove any residual oxygen. The sample was then subjected to pulses of 5% CO/Ar until the catalyst surface is saturated. The amount of CO is recorded during the pulse experiment using a 5975C Agilent Technologies mass spectrometer. Finally, the sample was flushed with Ar and cooled to room temperature.

XPS measurements were performed on an AXIS-165 manufactured by Kratos Analytical Inc. (Spring Valley, NY, USA) using achromatic X-ray radiation of 1487 eV (AlK $\alpha$ ) with a base pressure of  $8 \times 10^{-9}$  torr. The spectrometer was calibrated against both the Au 4f<sub>7/2</sub> peak at 84.0 eV and the Ag 3d<sub>5/2</sub> peak at 368.3 eV. Static charging was corrected with a neutralizer (flood gun) by placing the oxygen peak (O 1s) at about 529.3 eV. This binding energy of oxygen is for CZ that contains 68% Ce and 32% Zr. Curve fitting of the Ni 2p<sub>3/2</sub> and Mo 3d peaks were performed with the CasaXPS software, Ltd.

Electrochemical performance of the anode-supported coin-type single cell was measured using an electrochemical workstation (Metrohm Autolab M101) and a DC electric load (BK precision 8500). The experimental setup has been described in detail in the previous paper [22]. The single cell was heated to 800 °C and the anode was reduced in hydrogen. The open circuit voltage of the cell was recorded as a function of time. After the open circuit voltage of the cell reached a steady state, the temperature of the

cell was cooled down to 750 °C for electrochemical performance measurements. The performance of the single cell was first investigated using hydrogen (50 sccm hydrogen and 50 sccm nitrogen) as fuel. Then, the fuel was changed to a mixture of isooctane and air: 100 sccm air was fed through a bubbler containing isooctane at 25 °C [23]. Measurements were made once the open circuit voltage reached a stable condition.

### 2.3. Catalytic evaluation

The catalytic partial oxidation of isooctane (CPOX) was performed in an isothermal 7 mm fixed-bed tubular quartz reactor loaded with 0.1 g of catalyst held by a quartz wool plug. A K-type thermocouple was placed at the center of the catalyst bed to record and control its temperature. A silicon carbide bed was placed 5 cm apart from the catalyst bed inside the furnace to enhance the mixing of the reactants (Fig. 2). The reactant feed was composed of isooctane and air with an O<sub>2</sub>/C ratio of 0.4 introduced to the reactor at a flow rate of 3 ml/h and 100 sccm, respectively (gas hourly space velocity (GHSV) of 45,000 h<sup>-1</sup>) at atmospheric pressure and a temperature of 750 °C. The isooctane vaporizes once it enters the main reactor and a calibrated mass flow controller and syringe pump were used to control the flow rates of air and isooctane, respectively. The product stream was cooled to 5 °C to separate the condensable and gaseous products. The composition of the dry off-gas (H<sub>2</sub>, CO, CH<sub>4</sub>, CO<sub>2</sub>, C<sub>2</sub>H<sub>2</sub> and C<sub>2</sub>H<sub>4</sub>) was analyzed by an SRI gas chromatograph equipped with molecular sieve 13X and HayeSep D packed columns and thermal conductivity detector (TCD). The conversion of isooctane during CPOX was calculated according to Eq. (1). The H<sub>2</sub> and CO yields were calculated according to Eqs. (2) and (3), respectively.

$$\% \text{ Conversion} = \frac{\text{moles of (CO + CO}_2\text{ + CH}_4\text{) produced}}{8 * \text{moles of isooctane fed}} \quad (1)$$

$$\% \text{ H}_2 \text{ Yield} = \frac{2 * \text{moles of H}_2 \text{ produced}}{18 * \text{moles of isooctane fed}} \quad (2)$$

$$\% \text{ CO Yield} = \frac{\text{moles of CO produced}}{8 * \text{moles of isooctane fed}} \quad (3)$$

## 3. Results and discussion

### 3.1. Catalyst characterization

The BET surface areas of the catalyst are shown in Table 1. There was a slight decrease in the surface area with increasing Mo load-

**Table 1**  
BET surface area and metal dispersion data.

| Sample       | BET surface area (m <sup>2</sup> /g) | Metal Dispersion (%) |
|--------------|--------------------------------------|----------------------|
| CZ           | 40.3                                 | –                    |
| Ni-Mo(3%)/CZ | 36.8                                 | 15.2                 |
| Ni-Mo(2%)/CZ | 37.1                                 | 11.1                 |
| Ni-Mo(1%)/CZ | 37.5                                 | 10.5                 |
| Ni/CZ        | 38.7                                 | 9.9                  |

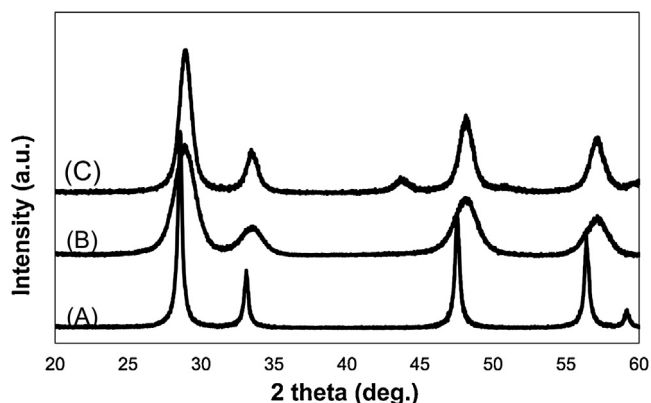


**Fig. 3.** X-ray diffraction profiles of CeO<sub>2</sub> (A), CZ (B), and Ni/CZ (C).

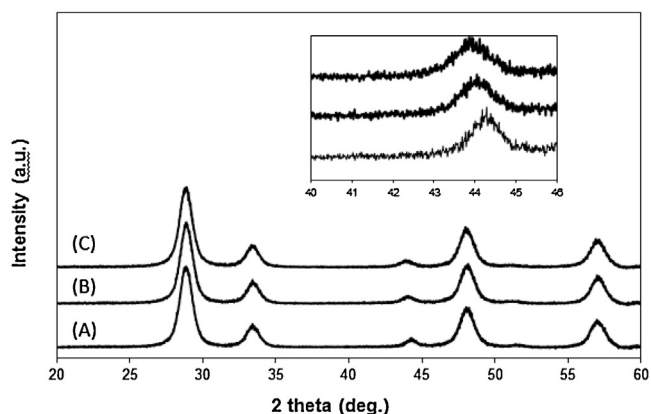


**Fig. 4.** X-ray diffraction profiles of Ni-Mo (1%)/CZ (A), Ni-Mo (2%)/CZ (B), and Ni-Mo (3%)/CZ (C).

ing. Fig. 3 presents XRD patterns of ceria, CZ and reduced Ni/CZ. The pattern for ceria matches with JCPDS No. 34-0394. No additional peaks were seen in the pattern from the CZ sample, which suggests that the ZrO<sub>2</sub> is incorporated into the CeO<sub>2</sub> lattice to form a solid solution [17,24,25]. The diffraction peaks are shifted to higher 2θ angles (from e.g., from 28.5° to 28.8°) with the addition of ZrO<sub>2</sub> because of the shrinkage of the lattice due to a partial substitution of Ce ions by the smaller Zr ions [18]. The average crystallite sizes of the support were calculated from XRD. The results showed that the average crystallite size of ceria was lowered by the addition of Zr from 26 nm to 11 nm (+/−2%). The Ni/CZ sample produced very broad and weak diffraction peaks corresponding to the Ni metal at 2θ = 44.2° and 51.5° suggesting that the Ni particles are well dispersed on the CZ solid solution. The phase structure of the reduced Ni-Mo/CZ with different Mo concentrations was also analyzed by XRD (Fig. 4). All samples clearly showed diffraction peaks corresponding to CeO<sub>2</sub>. Weak peaks due to Ni metal are visible while there are no peaks that can be assigned to Mo. However, with the addition of Mo, the diffraction peaks are shifted to lower 2θ angles. This observation is attributed to the expansion of the Ni lattice due

to a partial substitution of Ni atoms by the larger Mo atoms. Thus, a Ni-Mo solid solution is formed in the reduced Ni-Mo/CZ samples.

H<sub>2</sub>-TPR was used to study the reducibility and the interaction between the support and the metal (Fig. 5). TPR of commercial ceria shows two reduction peaks at 375 and 740 °C, which can be assigned to surface reduction and bulk reduction, respectively. The shrinkage of the lattice due to the substitution of the larger Ce ions (1.09 Å) by the smaller Zr ions (0.86 Å) induces a distortion of the oxygen sub-lattice and favors the migration of bulk oxygen to the surface [26]. Each cerium cation is coordinated by eight equivalent nearest-neighbor oxygen anions and the ionic radius of Zr<sup>4+</sup> is too small to accommodate all the oxygen anions [27]. Consequently, a lower reduction temperature and simultaneous reduction of both bulk and surface sites in a single TPR peak are observed as shown in Fig. 5 [28,29]. These defects also enhance the oxygen storage capacity (OSC) and cumulative oxygen storage capacity (COSC) of CZ as shown in Fig. 6 [27]. During the oxygen release process of pure ceria under the reducing environment, the oxidation state changes from Ce<sup>4+</sup> to Ce<sup>3+</sup> causing a volume expansion and a residual stress energy, which prevents further reduction and negatively affects its OSC. Introduction of Zr into the ceria compensates for the volume expansion, which may improve the OSC [30].

For the Ni/CZ catalyst, the reducibility of the cubic phase CZ support is further shifted down to lower temperature where the single CZ reduction peak is combined with the reduction peak of NiO to Ni metal. This trend suggests that the presence of Ni greatly improves the reducibility of the CZ support due to the improved H<sub>2</sub> dissociative adsorption rate over the metallic Ni sites followed by H spillover to the CZ support [31]. According to Fig. 5, as the Mo concentration increases, the reduction peaks of Ni-Mo/CZ catalysts are shifted to higher temperature than that of Ni/CZ catalysts suggesting that the Mo species can improve the metal-support interaction for the monometallic Ni species [32] and the Ni dispersion over CZ supports (see Table 1). TEM images and EDS data shown in Fig. 7 also indicate the good dispersion of Ni and Mo for the Ni-Mo (3%)/CZ sample.

### 3.2. Catalytic activity and stability for POX of isooctane

The catalytic activity and stability results for partial oxidation of isooctane over Ni-Mo/CZ catalysts are shown in Figs. 8 and 9 in terms of isooctane conversion and H<sub>2</sub> and CO yields, respectively. The reaction was carried out at conditions similar to those for the fuel cell experiments (T = 750 °C, P = 1 atm, isooctane and air flow rates of 3 ml/h and 100 sccm, respectively, and GHSV = 45000 h<sup>−1</sup>). According to Fig. 8, the Ni-Mo bimetallic catalyst shows higher initial conversion of isooctane and better stability than the monometallic Ni sample. The activity of Ni-Mo/CZ with 3 wt% Mo catalyst shows 100% isooctane conversion over 12 h on stream. On the other hand, the catalysts with lower Mo content experience severe deactivation after a few hours along with a pressure drop, which is due to carbon formation that plugs the reactor. Fig. 9 shows that the CO and H<sub>2</sub> yields for Ni-Mo/CZ with 3 wt% Mo are stable at 82 and 75%, respectively, over a 24 h run. The CO<sub>2</sub> and CH<sub>4</sub> yields are about 9 and 7% with insignificant production of C<sub>2</sub> compounds. For the reference, the blank run was also performed, which shows a performance of 32% conversion, 22% CO yield, and 5% H<sub>2</sub> yield. This result indicates that a Ni catalyst with 3 wt% Mo supported on CZ possesses superior activity and stability than that of a Ni monometallic catalyst (i.e., Ni/CZ). The stoichiometric ratio between H<sub>2</sub> and CO is 1.125 according to Eq. (4):



The actual molar ratio of H<sub>2</sub> to CO is about 0.92 for Ni-Mo (3%)/CZ sample based on Fig. 9, which is lower than the stoichiometric ratio. This difference indicates the occurrence of the reverse-water



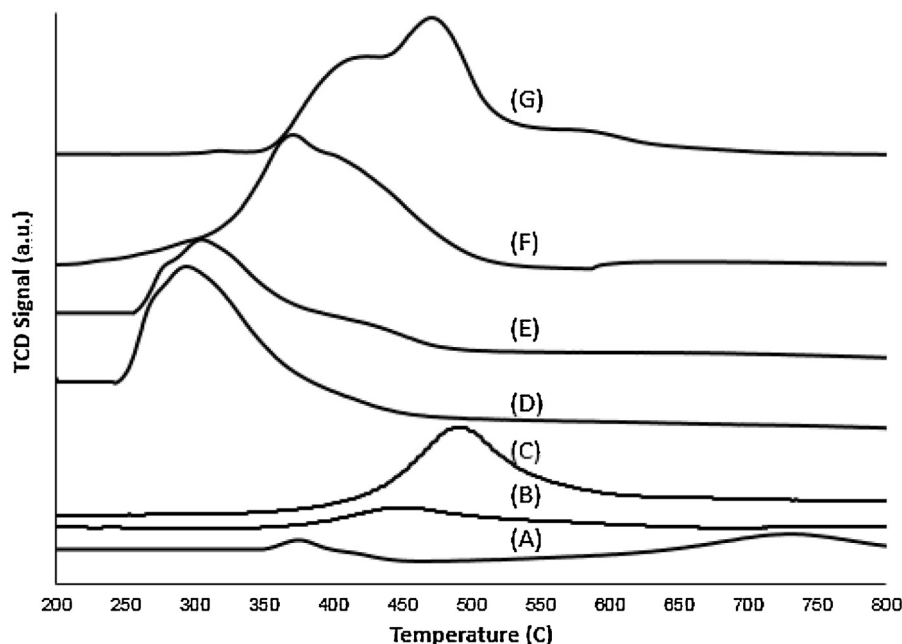


Fig. 5.  $H_2$  TPR of  $CeO_2$  (A), CZ (B),  $MoO_3/CZ$  (C),  $Ni/CZ$  (D),  $Ni-Mo(1\%)/CZ$  (E),  $Ni-Mo(2\%)/CZ$  (F) and  $Ni-Mo(3\%)/CZ$  (G).

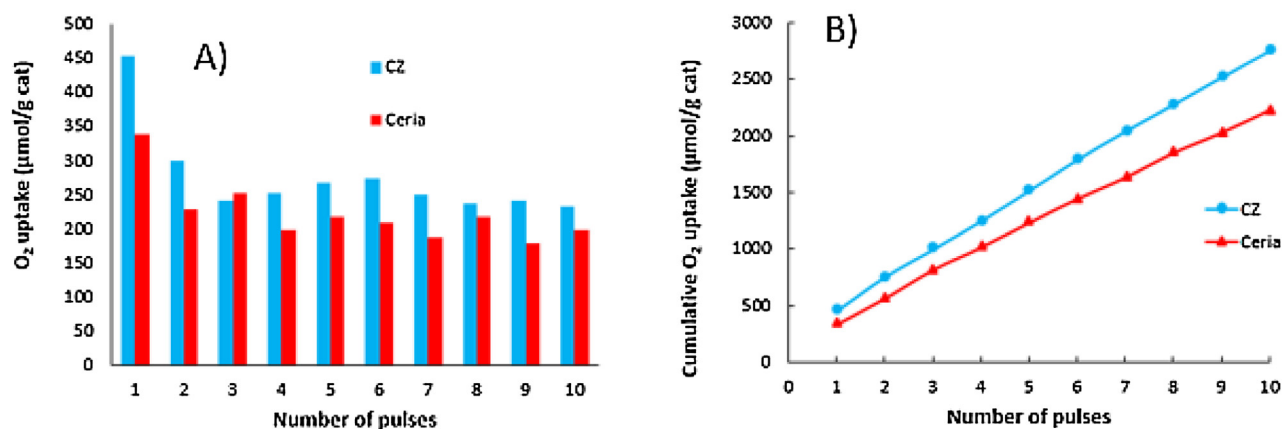
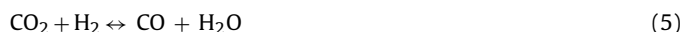


Fig. 6. Oxygen uptake amount per mass of catalysts as a function of pulse number (A) and Cumulative oxygen storage capacity (COSC) (B) for both the  $CeO_2$  and CZ supports.

gas shift (RWGS) reaction (Eq. (5)) that consumes some of the  $H_2$  produced during the partial oxidation process as follows:



The catalytic performance of the Ni-Mo catalyst with a Mo content greater than 3 wt% is similar to that of the 3 wt% samples (results are not shown here). Thus, Ni-Mo (3%)/CZ is the minimum amount of Mo needed to get superior activity and stability for partial oxidation of isooctane at high flow rates. Marin Flores et al. [33] reported that the performance of  $MoO_3$  for the partial oxidation of isooctane significantly decreases after 1 h on stream at  $O_2/C$  of 0.41 (same ratio used for this study) because of the formation of  $Mo_2C$  [34]. Unlike these two previous studies, this present work has utilized Mo as the promotor for the Ni/CZ catalytic system to enhance its overall reforming performances toward isooctane.

The initial effect of the added Mo is that it improves the dispersion of Ni and retards sintering. The catalytic activity and stability of Ni is determined by its dispersion and interaction with the support [35]. A low metallic dispersion of supported Ni catalysts has been recognized as one of the reasons for the severe carbon deposition that takes place with Ni-based catalysts during fuel reforming

[36]. It has been demonstrated that highly dispersed Ni nanoparticles over the support surface exhibit much improved reforming activity, higher stability and lower coke formation [37]. The XRD data for Ni-Mo(3%)/CZ sample shows very broad diffraction peaks corresponding to Ni, which indicates that the Ni is well dispersed over the CZ support [38]. Our TEM/EDS data also confirms the presence of highly dispersed Ni nanoparticles over the support surface for the Ni-Mo (3%)/CZ sample. A strong metal-support interaction (SMSI) promoted by the presence of Mo would be responsible for the high dispersion of Ni nanoparticles [39]. Our TPR reduction peak shifts also suggest a greater SMSI and better Ni dispersion. These factors should provide a high resistance for coking because of the limited mobility of the Ni species on the support [40].

The prevention of Ni nanoparticle growth is a very critical step in order to mitigate coking during fuel reforming because carbon nucleation requires a large ensemble of Ni sites to produce coke [41]. The presence of Mo maintains the small size of the Ni particles as shown in Fig. 7 and this lowers the tendency for growth of the Ni nanoparticles to the point where they can facilitate coke formation. Tin (Sn) is another element that has been introduced to Ni in order to reduce the ensemble size and prevent surface coking

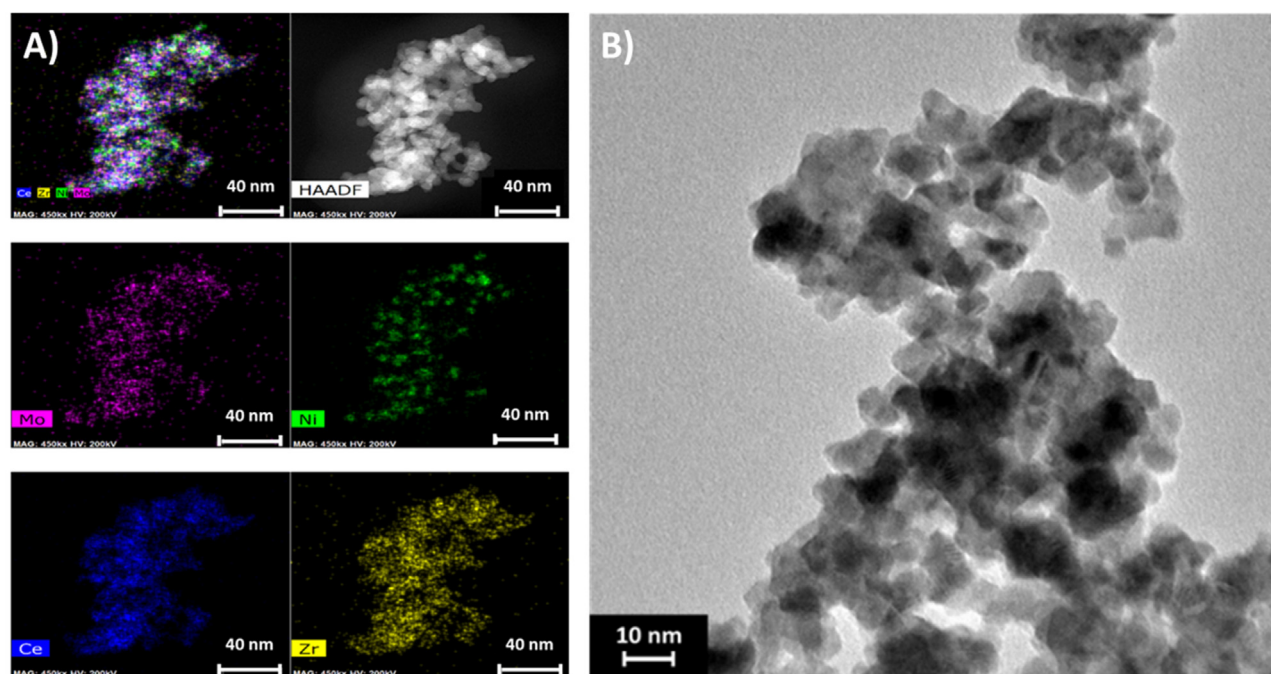


Fig. 7. Scanning transition electron microscopy with EDS of Ni-Mo (3%)/CZ sample (A) and its transition electron microscopy (B).

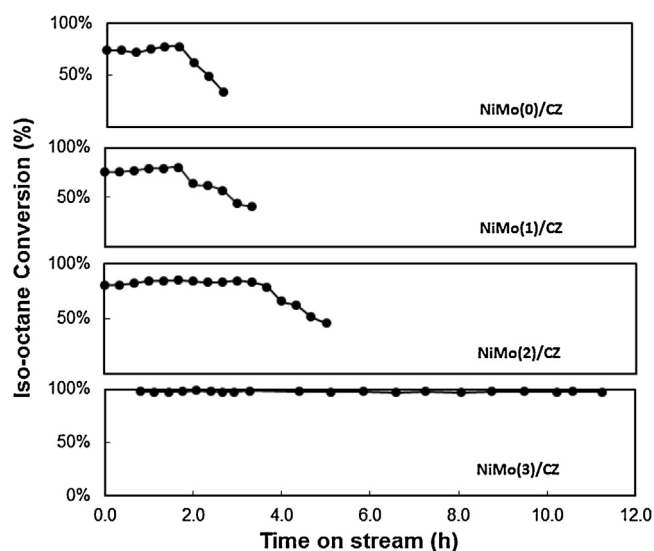


Fig. 8. Catalytic activity of the Ni-Mo/CZ catalysts with different amounts of Mo for isooctane partial oxidation at air and fuel flow rates of 100 sccm and 3 ml/h, respectively, temperature of 750 °C and O<sub>2</sub>/C ratio of 0.4.

[42]. A similar explanation has been proposed for Ni-Mo and Co-Mo systems where the effect of the Mo species leads to the size reduction of Ni and Co particles and the prevention of surface coking [43]. Huang et. al [39] reported that Mo species play an important role in reducing the amount of shell-like carbon deposition, which could encapsulate the Ni particles. According to this previous study, the SMSI not only leads to the high dispersion of Ni nanoparticles, but it also prevents Ni-Mo metal particles being physically lifted up from the support during the carbon growth process and limits the encapsulation of the Ni particles by carbon [44]. The XRD patterns of the fresh and spent Ni-Mo (3%)/CZ and Ni/CZ samples are shown in Fig. 10. The spent Ni-Mo sample showed insignificant differences with those for the fresh samples (with crystallite size ~6 nm), implying that the Ni-Mo metallic phase was well dis-

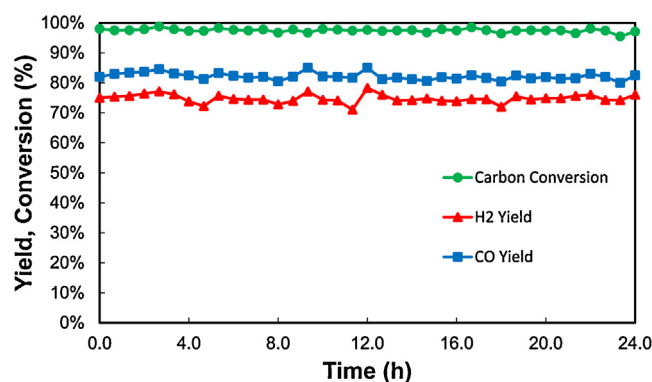


Fig. 9. Isooctane conversion and the yields of H<sub>2</sub> and CO for the Ni-Mo (3%)/CZ catalyst toward isooctane partial oxidation reaction at air and fuel flow rates of 100 sccm and 3 ml/h, respectively, temperature of 750 °C and O<sub>2</sub>/C ratio of 0.4.

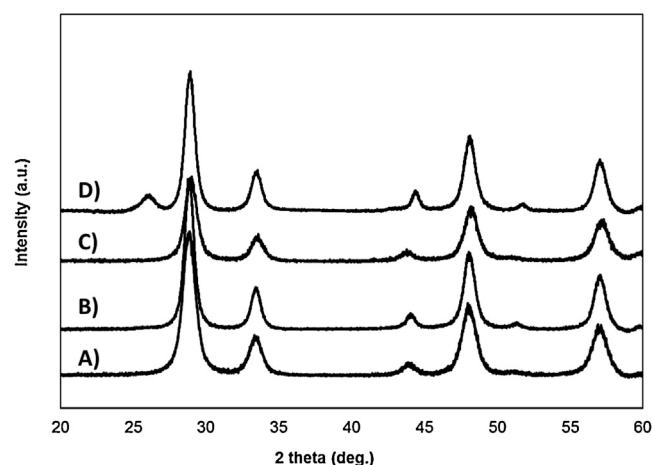


Fig. 10. XRD patterns of fresh Ni-Mo (3%)/CZ (A), spent Ni-Mo (3%)/CZ (B), fresh Ni/CZ samples (C) and spent Ni/CZ samples (D). The operation time for Ni-Mo (3%)/CZ sample was 24 hours, while that of Ni/CZ sample was less than 4 hours due to its severe coking and pressure drop.

**Table 2**  
XPS data summary.

| Elements             | Samples                         |                                |
|----------------------|---------------------------------|--------------------------------|
|                      | Ni/CZ                           | NiMo (3%)/CZ                   |
| *O 1s                | 529.3 eV                        | 529.3 eV                       |
| Ni 2p <sub>3/2</sub> | 851.6 eV (Ni)                   | 851.9 eV (Ni)                  |
|                      | 853.7 eV (NiO)                  | 853.8 eV (NiO)                 |
|                      | 855.7 eV (Ni(OH) <sub>2</sub> ) | 855.0 eV (NiMoO <sub>4</sub> ) |
| Mo 3d <sub>5/2</sub> | –                               | 228.0 eV (Mo)                  |
|                      | –                               | 231.9 eV (NiMoO <sub>4</sub> ) |

\*Static charging was corrected by placing the oxygen peak (O 1s) at about 529.3 eV.

persed over the CZ support and demonstrates a high resistance for agglomeration under the severe reaction conditions. Moreover, there is no diffraction peak at  $2\theta = 26^\circ$  indicating that there is no graphitic carbon formation during isoctane reforming over 24 h, which is also confirmed by TGA data (not shown). Unlike the Ni-Mo (3%)/CZ samples, the monometallic Ni on CZ sample (i.e., Ni/CZ) shows the formation of graphitic carbon that caused a large pressure buildup in the reactor bed and rapid deactivation during partial oxidation conditions. Based on Fig. 10 and applying Scherrer's equation, we estimate that the average crystalline sizes of Ni are 4.9, 6.2, 6.1, and 9.4 nm for fresh Ni-Mo (3%)/CZ, spent Ni-Mo (3%)/CZ, fresh Ni/CZ, and spent Ni/CZ samples, respectively. Thus, XRD data shows a bigger average Ni crystallite size for Ni/CZ sample compared to that of Ni-Mo (3%)/CZ sample following the partial oxidation reaction, which indicates that the higher degree of sintering took place for the sample without Mo. The effect of Mo species on Ni particle sintering and carbon formation is also clearly demonstrated by comparing the TEM images of both Ni-Mo (3%)/CZ and Ni/CZ samples before and after the reforming reaction (see Supporting Information). As shown in the TEM images, Ni nanoparticles are well dispersed over the CZ support regardless of the presence of Mo species before the reforming tests. However, the spent Ni/CZ sample shows a significant degree of sintering and carbon deposition. Unlike the Ni/CZ sample, the TEM image of the spent Ni-Mo (3%)/CZ sample shows no evidence of particle sintering and an absence of coking.

The second effect of introducing Mo to Ni/CZ samples is that it alters the electronic property of Ni clusters. When the bonding energy (BE) of Ni 2p<sub>3/2</sub> is compared between Ni/CZ and Ni-Mo (3%)/CZ samples (Table 2), the value increased by 0.3 eV with the introduction of the Mo species. It is well known that the electronic property of supported Ni clusters can be tuned by dopant additions [45]. The occurrence and the direction of charge transfer is not always easy to predict and it depends on the nature of the adsorbed atoms and the dopant, their ionization potential and electron affinity, and their location on the supporting material. However, it is reasonable to assume that adding Mo, which has a higher electronegativity than Ni, would facilitate additional electron donation from the Ni cluster to the Mo site and promote the formation of a Ni/Ni<sup>δ+</sup> redox couple for the Ni-Mo/CZ samples. Che et al. [46] used DFT calculations to show that the local positive oxidation state on Ni increases both the reaction energy and the activation energy of CH dissociation ( $\text{CH}^* \rightarrow \text{C}^* + \text{H}^*$ ), consequently the formation of carbon deposits will be impeded with the positively charged state of the Ni clusters. Furthermore, the same study shows that the kinetic parameters for hydrocarbon oxidation could be significantly influenced by the local oxidation state of Ni. Hence, the modification of the local Ni oxidation state by the addition of Mo as the promoter could be responsible for the enhanced reforming performance of Ni-Mo (3%)/CZ samples.

The third effect of introducing Mo to Ni/CZ samples is the formation of surface NiMoO<sub>4</sub> species. The presence of this compound is

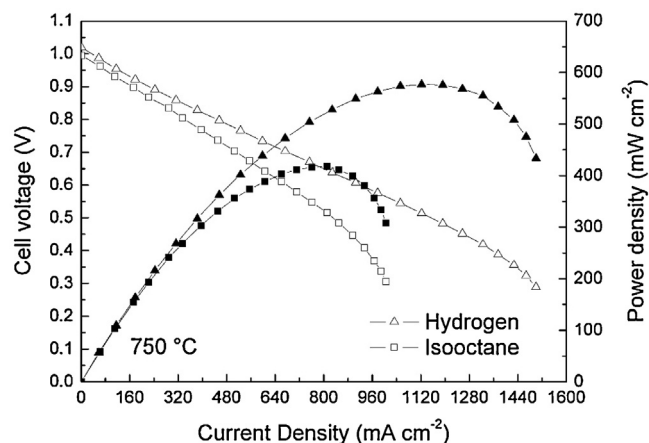


**Fig. 11.** I–V plots of the Ni-YSZ anode-based SOFC with the Ni-Mo (3%)/CZ catalyst layer under hydrogen and isoctane operation modes at 750 °C.

confirmed by XPS analysis. Peak binding energies (BE) and their assignments are summarized in Table 2. XPS analysis of Ni-Mo (3%)/CZ samples display three peaks for Ni 2p located at BE = 851.9, 853.9, and 855.0 eV, which are assigned to elemental Ni, NiO, and NiMoO<sub>4</sub>, respectively (see Fig. S2). The formation of NiMoO<sub>4</sub> from the reaction between MoO<sub>3</sub> and NiO phases during calcination has been reported for the Ni-Mo system [47]. To validate the presence of NiMoO<sub>4</sub> in the Ni-Mo (3%)/CZ sample, we also analyzed the Mo 3d XPS spectrum. Two different types of surface Mo species were detected; a weak peak located at 228 eV assigned to Mo metal, an intense peak at 231.9 eV assigned to Mo<sup>6+</sup>. The latter is present in NiMoO<sub>4</sub> [48,49]. The assignments of Ni 2p peaks for Ni-Mo/CZ were compared to those for Ni/CZ. The peak at BE = 855.7 eV for Ni/CZ sample corresponds to Ni(OH)<sub>2</sub> which was not detected in Ni-Mo/CZ. The deconvoluted Ni 2p signal shown in Fig. S2 displays a more intense NiMoO<sub>4</sub> signal than the Ni(OH)<sub>2</sub> signal. The relative concentration of NiMoO<sub>4</sub> is 32 at% of the total Ni presented in the Ni-Mo/CZ sample, but only 9 at% for Ni(OH)<sub>2</sub> in the Ni/CZ sample (Fig. S2). Interestingly, the amount of NiO decreases with the addition of Mo from 63.2 at% to 30.8 at% in the sample to form additional Ni metal and NiMoO<sub>4</sub> phases for the Ni-Mo/CZ sample. The formation of NiMoO<sub>4</sub> can hinder coke formation [50]. Hou et al. [51] reported a similar effect in that the formation of an intermetallic alloy of Ni and Sn (such as Ni<sub>3</sub>Sn) can prevent coking. Other researchers reported the catalytic activity of NiMoO<sub>4</sub> in hydrocarbon reforming. Shah et al. [21] suggested that the formation of a Ni-Mo solid solution can enhance hydrocarbon reforming activity. Gharibi et al. [50] reported that the high activity of the Ni-Mo system is attributed to the existence of a NiMoO<sub>4</sub> phase and higher metal dispersion. The formation of NiMoO<sub>4</sub> results in the electron transfer from the Ni cluster to Mo leading to an electron-deficient state of the Ni species [50]. As in case of Ni clusters with the Ni<sup>δ+</sup> state, the presence of this Ni species in the form of NiMoO<sub>4</sub> with the electron-deficient state could contribute to the enhancement of reforming performance for the Ni-Mo (3%)/CZ sample.

#### 4.1. SOFC fabrication and performance

We fabricated a Ni-YSZ anode-based SOFC with the catalytic reforming layer using Ni-Mo (3%)/CZ samples (See Fig. 1). Fig. 11 shows the cell voltage and power density curves as a function of current density at 750 °C using H<sub>2</sub> and isoctane/air mixture as the fuel, respectively. The cell exhibited an open circuit voltage of 1.02 V and a maximum power density of 577 mW cm<sup>-2</sup> with H<sub>2</sub> fuel. The data was comparable with previously published results on a Ni-containing anode supported single cell [52,53].



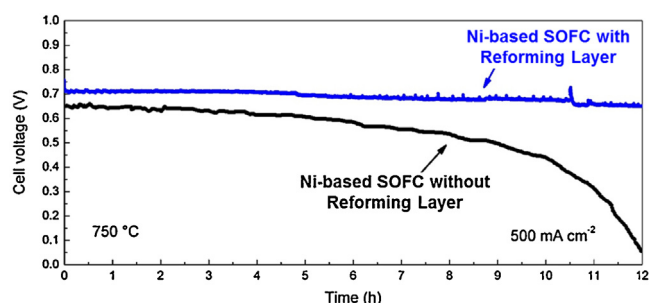


Fig. 12. Performance stability of the Ni-YSZ anode-based SOFC with the Ni-Mo (3%)/CZ catalyst layer at the constant current density of  $500 \text{ mA cm}^{-2}$ .

When the fuel was switched from  $\text{H}_2$  to isooctane/air, the open circuit voltage dropped from 1.02 to 1.00 V. We expect that the isooctane would go through the thermal decomposition process and be fragmented into small hydrocarbons (e.g.,  $\text{C}_1$ – $\text{C}_4$  species) before it reaches the reforming layer on the anode. Hartman et al. [54] analyzed the product stream from the POX of isooctane using FT-IR, GC/MS and a paramagnetic gas analysis. Another detailed chemical kinetic mechanism for the POX of isooctane was developed by the combustion group at Lawrence Livermore National Laboratory (LLNL) [55]. The proposed gas-phase mechanism consists of 7193 irreversible reactions among 857 species [55]. Despite this thermal decomposition and fragmentation of isooctane, it is very important to point out that our main fuel source is still isooctane, which is comparable to other groups' works using isooctane as the fuel [56].

The variation of open circuit potential could be due to the differences of gas compositions in the anode. In addition, the maximum power density of the single cell decreased from 557 to  $419 \text{ mW cm}^{-2}$ . The feeding of isooctane/air would lead to a decreased  $\text{H}_2$  concentration and increased CO in the anode (see Fig. 9). As the CO electrochemical oxidation reaction rate is slower compared with that of  $\text{H}_2$ , the changes of fuel composition in the anode could reduce the maximum power density of the single cell [57].

To study the effect of the catalytic reforming layer on performance stability of the Ni-YSZ anode-based SOFC under the isooctane/air operation mode, its performance was measured at constant current density of  $500 \text{ mA cm}^{-2}$  at  $750^\circ\text{C}$  (Fig. 12). The single cell without the catalyst layer showed an unstable voltage and the overall cell performance exhibited a rapid degradation rate of  $49 \text{ mV/h}$  after 6 h of operation. The fast degradation could be due to carbon deposition in the anode [56]. By applying the catalytic reforming layer, the single cell displayed significantly improved stability with a low degradation rate of  $4.8 \text{ mV h}^{-1}$  during the 12 h test. The improved performance stability denoted the positive function of the catalytic layer for efficiently reforming complex hydrocarbon fuels in the anode and suppressing carbon deposition.

## 5. Conclusion

We have synthesized Ni-Mo bimetallic catalysts with different weight % of Mo species supported on CZ using the co-impregnation method. Our catalyst studies demonstrate that Ni-Mo (3%)/CZ samples possess an excellent catalytic performance for the partial oxidation of isooctane in terms of carbon conversion (100%) and  $\text{H}_2$  yield (75%) using high space velocities of fuel. More importantly, Ni-Mo (3%)/CZ samples show much improved coking resistance compared to samples without Mo. The presence of Mo (1) enhances the interaction between the Ni nanoparticles and the CZ support, which hinders their sintering rate; (2) modifies the electronic property of Ni clusters as it facilitates the charge transfer from the Ni

to Mo, which leads to the formation of the  $\text{Ni}^{\delta+}$  state; and (3) promotes the formation of surface  $\text{NiMoO}_4$  species that is known for its high fuel reforming activity and stability. We believe that these combined effects allow Ni-Mo (3%)/CZ samples to show high performance toward the partial oxidation of isooctane. Furthermore, Ni-Mo (3%)/CZ catalysts were applied as the reforming layer over conventional Ni-YSZ anode-based SOFCs. Under the isooctane/air mixture operating mode, an initial maximum power density of  $419 \text{ mW cm}^{-2}$  was achieved together with high stability and much improved coking resistance compared to the Ni-based SOFC without the reforming layer. The excellent catalytic activity, stability, coking resistance, and low price of the Ni-Mo catalyst on CZ support under the harsh operating conditions reveal its promise as a high performance reforming layer for internal reforming SOFC applications operating with complex hydrocarbon fuels.

## Acknowledgements

This work was financially supported by the Office of Naval Research (Grant No. N00014-15-1-2416). We thank the Murdock Charitable Trust for their financial support for the upgrade of our existing XPS system. We thank the Franceschi Microscopy and Imaging Center at Washington State University for use of their facilities. We also would like to show our gratitude to Jake Gray at Washington State University for taking the TEM images.

## Appendix A. Supplementary data

Supplementary data associated with this article can be found, in the online version, at <http://dx.doi.org/10.1016/j.apcatb.2017.04.055>.

## References

- [1] H.C. Ong, T.M.I. Mahlia, H.H. Masjuki, A review on energy pattern and policy for transportation sector in Malaysia, *Renew. Sustain. Energy Rev.* 16 (2012) 532–542.
- [2] J. Rogelj, M. den Elzen, N. Höhne, T. Fransen, H. Fekete, H. Winkler, et al., Paris Agreement climate proposals need a boost to keep warming well below  $2^\circ\text{C}$ , *Nature* 534 (7609) (2016) 631–639.
- [3] C. Palm, D. Stolten, R. Peters, R. Dahl, U. Klu, Internal reforming of methane in solid oxide fuel cell systems, *J. Power Sources* 106 (2002) 238–244.
- [4] Z. Zhan, S.A. Barnett, An octane-Fueled solid oxide fuel cell, *Science* 308 (May) (2005) 844–848.
- [5] N.Q. Minh, Solid oxide fuel cell technology – features and applications, *Solid State Ion.* 174 (2004) 271–277.
- [6] D. Mogensen, J.D. Grunwaldt, P.V. Hendriksen, K. Dam-Johansen, J.U. Nielsen, Internal steam reforming in solid oxide fuel cells: status and opportunities of kinetic studies and their impact on modelling, *J. Power Sources* 196 (1) (2011) 25–38.
- [7] Y. Shiratori, T. Ijichi, T. Oshima, K. Sasaki, Internal reforming SOFC running on biogas, *Int. J. Hydrogen Energy* 35 (15) (2010) 7905–7912.
- [8] K. Kendall, M. Slinn, J. Preece, Formulating liquid ethers for microtubular SOFCs, *J. Power Sources* 157 (2) (2006) 750–753.
- [9] Z.F. Zhou, R. Kumar, S.T. Thakur, L.R. Rudnick, H. Schobert, S.N. Lvov, Direct oxidation of waste vegetable oil in solid-oxide fuel cells, *J. Power Sources* 171 (2) (2007) 856–860.
- [10] S. Wang, G.Q.M. Lu, CO<sub>2</sub> reforming of methane on Ni catalysts: effects of the support phase and preparation technique, *Appl. Catal. B Environ.* 16 (3) (1998) 269–277.
- [11] S. Li, J. Gong, P. Ferreira-Aparicio, M.J. Benito, J.L. Sanz, E. McFarland, et al., Strategies for improving the performance and stability of Ni-based catalysts for reforming reactions, *Chem. Soc. Rev.* 43 (21) (2014) 7245–7256.
- [12] E.C. Vagia, A.A. Lemonidou, Investigations on the properties of ceria-zirconia-supported Ni and Rh catalysts and their performance in acetic acid steam reforming, *J. Catal.* 269 (2) (2010) 388–396.
- [13] L.V. Mattos, E. Rodino, D.E. Resasco, F.B. Passos, F.B. Noronha, Partial oxidation and CO<sub>2</sub> reforming of methane on Pt/Al<sub>2</sub>O<sub>3</sub>, Pt/ZrO<sub>2</sub>, and Pt/Ce-ZrO<sub>2</sub> catalysts, *Fuel Process. Technol.* 83 (1–3 special) (2003) 147–161.
- [14] F. Silva, J.A.C. Ruiz, K.R. de Souza, J.M.C. Bueno, L.V. Mattos, F.B. Noronha, et al., Partial oxidation of methane on Pt catalysts: effect of the presence of ceria-zirconia mixed oxide and of metal content, *Appl. Catal. A Gen.* 364 (1–2) (2009) 122–129.



- [15] A. Wolfbeisser, O. Sophiphun, J. Bernardi, J. Wittayakun, K. Föttinger, G. Rupprechter, Methane dry reforming over ceria-zirconia supported Ni catalysts, *Catal. Today* 277 (2016) 234–245.
- [16] X. Xiang, H. Zhao, J. Yang, J. Zhao, L. Yan, H. Song, et al., Nickel based mesoporous silica-ceria-zirconia composite for carbon dioxide reforming of methane, *Appl. Catal. A Gen.* 520 (2016) 140–150.
- [17] E. Moretti, L. Storaro, A. Talon, S. Chitsazan, G. Garbarino, G. Busca, et al., Ceria-zirconia based catalysts for ethanol steam reforming, *Fuel* 153 (2015) 166–175.
- [18] S. Xu, X. Wang, Highly active and coking resistant Ni/CeO<sub>2</sub>-ZrO<sub>2</sub> catalyst for partial oxidation of methane, *Fuel* 84 (5) (2005) 563–567.
- [19] C.E. Quincoces, S.P. De Vargas, P. Grange, M.G. González, Role of Mo in CO<sub>2</sub> reforming of CH<sub>4</sub> over Mo promoted Ni/Al<sub>2</sub>O<sub>3</sub> catalysts, *Mater. Lett.* 56 (5) (2002) 698–704.
- [20] S. Shah, O.G. Marin-Flores, K. Chinnathambi, M.G. Norton, S. Ha, Partial oxidation of surrogate jet-A fuel over SiO<sub>2</sub> supported MoO<sub>3</sub>, *Appl. Catal. B Environ.* (2016) 193.
- [21] S. Shah, O.G. Marin-Flores, M.G. Norton, S. Ha, Molybdenum carbide supported nickel-molybdenum alloys for synthesis gas production via partial oxidation of surrogate biodiesel, *J. Power Sources* 294 (2015) 530–536.
- [22] K. Zhao, Y. Du, Calcium-doped ceria materials for anode of solid oxide fuel cells running on methane fuel, *J. Power Sources* 347 (2017) 79–85.
- [23] Z. Zhan, S.A. Barnett, Solid oxide fuel cells operated by internal partial oxidation reforming of iso-octane, *J. Power Sources* 155 (2) (2006) 353–357.
- [24] E. Moretti, L. Storaro, A. Talon, M. Lenarda, P. Riello, R. Frattini, et al., Effect of thermal treatments on the catalytic behaviour in the CO preferential oxidation of a CuO-CeO<sub>2</sub>-ZrO<sub>2</sub> catalyst with a flower-like morphology, *Appl. Catal. B Environ.* 102 (3–4) (2011) 627–637.
- [25] E. Moretti, M. Lenarda, P. Riello, L. Storaro, A. Talon, R. Frattini, et al., Influence of synthesis parameters on the performance of CeO<sub>2</sub>-CuO and CeO<sub>2</sub>-ZrO<sub>2</sub>-CuO systems in the catalytic oxidation of CO in excess of hydrogen, *Appl. Catal. B Environ.* 129 (2013) 556–565.
- [26] S. Pengpanich, V. Meeyoo, T. Risksomboon, K. Bunyakiat, Catalytic oxidation of methane over CeO<sub>2</sub>-ZrO<sub>2</sub> mixed oxide solid solution catalysts prepared via urea hydrolysis, *Appl. Catal. A Gen.* 234 (1–2) (2002) 221–233.
- [27] E. Aneggi, M. Boaro, C. De Leitenburg, G. Dolcetti, A. Trovarelli, Insights into the redox properties of ceria-based oxides and their implications in catalysis, *J. Alloys Compd.* (2006) 1096–1102.
- [28] A. Scarabello, D. Dalle Nogare, P. Canu, R. Lanza, Partial oxidation of methane on Rh/ZrO<sub>2</sub> and Rh/Ce-ZrO<sub>2</sub> on monoliths: catalyst restructuring at reaction conditions, *Appl. Catal. B Environ.* 174–175 (2015) 308–322.
- [29] T.A. Maia, E.M. Assaf, Catalytic features of Ni supported on CeO<sub>2</sub>-ZrO<sub>2</sub> solid solution in the steam reforming of glycerol for syngas production, *RSC Adv.* 4 (59) (2014) 31142.
- [30] X. Wu, X. Wu, Q. Liang, J. Fan, D. Weng, Z. Xie, et al., Structure and oxygen storage capacity of Pr/Nd doped CeO<sub>2</sub>-ZrO<sub>2</sub> mixed oxides, *Solid State Sci.* 9 (7) (2007) 636–643.
- [31] D.W. Jeong, W.J. Jang, J.O. Shim, H.S. Roh, I.H. Son, S.J. Lee, The effect of preparation method on the catalytic performance over superior MgO-promoted Ni-CeO<sub>2</sub>-ZrO<sub>2</sub> catalyst for CO<sub>2</sub> reforming of CH<sub>4</sub>, *Int. J. Hydrogen Energy* 38 (31) (2013) 13649–13654.
- [32] T. Borowiecki, A. Golebiowski, B. Stasinska, Effects of small MoO<sub>3</sub> additions on the properties of nickel catalysts for the steam reforming of hydrocarbons, *Appl. Catal. A Gen.* 153 (1–2) (1997) 141–156.
- [33] O.G. Marin Flores, S. Ha, Activity and stability studies of MoO<sub>2</sub> catalyst for the partial oxidation of gasoline, *Appl. Catal. A Gen.* 352 (1–2) (2009) 124–132.
- [34] C.M. Cuba-Torres, O. Marin-Flores, C.D. Owen, Z. Wang, M. Garcia-Perez, M.G. Norton, et al., Catalytic partial oxidation of a biodiesel surrogate over molybdenum dioxide, *Fuel* 146 (2015) 132–137.
- [35] M. Montes, C. Penneman de Bosscheyde, B.K. Hodnett, F. Delannay, P. Grange, B. Delmon, Influence of metal-support interactions on the dispersion, distribution, reducibility and catalytic activity of Ni/SiO<sub>2</sub> catalysts, *Appl. Catal.* 12 (4) (1984) 309–330.
- [36] W. Yang, D. He, Role of poly(N-vinyl-2-pyrrolidone) in Ni dispersion for highly-dispersed Ni/SBA-15 catalyst and its catalytic performance in carbon dioxide reforming of methane, *Appl. Catal. A Gen.* 524 (2016) 94–104.
- [37] Z. Hou, T. Yashima, Meso-porous Ni/Mg/Al catalysts for methane reforming with CO<sub>2</sub>, *Appl. Catal. A Gen.* 261 (2) (2004) 205–209.
- [38] J. Guo, H. Lou, H. Zhao, D. Chai, X. Zheng, Dry reforming of methane over nickel catalysts supported on magnesium aluminate spinels, *Appl. Catal. A Gen.* 273 (1–2) (2004) 75–82.
- [39] T. Huang, W. Huang, J. Huang, P. Ji, Methane reforming reaction with carbon dioxide over SBA-15 supported Ni-Mo bimetallic catalysts, *Fuel Process. Technol.* 92 (10) (2011) 1868–1875.
- [40] S.B. Wang, G.Q.M. Lu, CO<sub>2</sub> reforming of methane on Ni catalysts: effects of the support phase and preparation technique, *Appl. Catal. B-Environ.* 16 (3) (1998) 269–277.
- [41] J.R. Rostrup-Nielsen, I. Alstrup, Innovation and science in the process industry: steam reforming and hydrogenolysis, *Catal. Today* 53 (3) (1999) 311–316.
- [42] Eranda Nikolla, Johannes Schwank, S. Linic, Promotion of the long term stability of reforming Ni catalysts by surface alloying, *J. Catal.* 250 (1) (2007) 85–93.
- [43] A.E. Aksoylu, Z. Mısırlı, Z.İ. Önsan, Interaction between nickel and molybdenum in Ni-Mo/Al<sub>2</sub>O<sub>3</sub> catalysts: I: CO<sub>2</sub> methanation and SEM-TEM studies, *Appl. Catal. A Gen.* 168 (2) (1998) 385–397.
- [44] R. Baker, Catalytic growth of carbon filaments, *Carbon N. Y.* 27 (3) (1989) 315–323.
- [45] E.W. McFarland, H. Metiu, Catalysis by doped oxides, *Chem. Rev.* 113 (2013) 4391–4427.
- [46] Fanglin Che, Jake T. Gray, Su Ha, J.S. McEwen, Improving Ni catalysts using electric fields: a DFT and experimental study of the methane steam reforming reaction, *ACS Catal.* 7 (1) (2016) 551–562.
- [47] R. Hernandez-Huesca, J. Merida-Robles, P. Maireles-Torres, E. Rodriguez-Castellon, A. Jimenez-Lopez, Hydrogenation and ring-opening of tetralin on Ni and NiMo supported on alumina-pillared alpha-zirconium phosphate catalysts. A thiotolerance study, *J. Catal.* 203 (1) (2001) 122–132.
- [48] F. Liu, S. Xu, L. Cao, Y. Chi, T. Zhang, D. Xue, A comparison of NiMo/Al<sub>2</sub>O<sub>3</sub> catalysts prepared by impregnation and coprecipitation methods for hydrodesulfurization of dibenzothiophene, *J. Phys. Chem. C* 111 (20) (2007) 7396–7402.
- [49] U.S. Ozkan, L. Zhang, S. Ni, E. Moctezuma, Investigation of the role of nickel and the effect of gas phase sulfur compounds on the performance of Ni-Mo/Al<sub>2</sub>O<sub>3</sub> hydrodenitrogenation catalysts, *J. Catal.* 148 (1) (1993) 181–193.
- [50] Abolfazl Gharibi Kharaji, Ahmad Shariati, M.O. Ostadi, Development of Ni-Mo/Al<sub>2</sub>O<sub>3</sub> catalyst for reverse water gas shift (RWGS) reaction, *J. Nanosci. Nanotechnol.* 14 (9) (2014) 6841–6847.
- [51] Z. Hou, O. Yokota, T. Tanaka, T. Yashima, Surface properties of a coke-free Sn doped nickel catalyst for the CO<sub>2</sub> reforming of methane, *Appl. Surf. Sci.* 233 (1–4) (2004) 58–68.
- [52] M. Chen, B.H. Moon, S.H. Kim, B.H. Kim, Q. Xu, B.G. Ahn, Characterization of La<sub>0.6</sub>Sr<sub>0.4</sub>Co<sub>0.2</sub>Fe<sub>0.8</sub>O<sub>3-δ</sub> + La<sub>2</sub>NiO<sub>4</sub> + δ composite cathode materials for solid oxide fuel cells, *Fuel Cells* 12 (1) (2012) 86–96.
- [53] K. Zhao, Y.-P. Wang, M. Chen, Q. Xu, B.-H. Kim, D.-P. Huang, Electrochemical evaluation of La<sub>2</sub>NiO<sub>4</sub> + δ as a cathode material for intermediate temperature solid oxide fuel cells, *Int. J. Hydrogen Energy* 39 (13) (2014) 7120–7130.
- [54] M. Hartmann, L. Maier, H.D. Minh, O. Deutschmann, Catalytic partial oxidation of iso-octane over rhodium catalysts: an experimental, modeling, and simulation study, *Combust. Flame* 157 (9) (2010) 1771–1782.
- [55] H.J. Curran, P. Gaffuri, W.J. Pitz, C.K. Westbrook, A comprehensive modeling study of iso-octane oxidation, *Combust. Flame* 129 (3) (2002) 253–280.
- [56] Z. Zhan, S.A. Barnett, Operation of ceria-electrolyte solid oxide fuel cells on iso-octane-air fuel mixtures, *J. Power Sources* 157 (1) (2006) 422–429.
- [57] X.F. Ye, S.R. Wang, J. Zhou, F.R. Zeng, H.W. Nie, T.L. Wen, Assessment of the performance of Ni-yttria-stabilized zirconia anodes in anode-supported solid oxide fuel cells operating on H<sub>2</sub>-CO syngas fuels, *J. Power Sources* 195 (21) (2010) 7264–7267.